Science of the Total Environment 913 (2024) 169750

Contents lists available at ScienceDirect

Science of the Total Environment

journal homepage: www.elsevier.com/locate/scitotenv

Impact of unrecovered shale gas reserve on methane emissions from abandoned shale gas wells

Yun Yang [a,b], Shimin Liu [a,*], Haoming Ma [b]

[a] Department of Energy and Mineral Engineering, G3 Center and EMS Energy Institute, The Pennsylvania State University, University Park, PA 16802, USA
[b] University of Calgary, Calgary, Alberta T2N 1N4, Canada

HIGHLIGHTS

- Contributions of Knudsen diffusion, slip and viscous flow to total mass transfer strongly depend on shale matrix pressure.
- Knudsen diffusion is the primary mechanism for methane emissions from abandoned shale gas wells (~ 20 × 10^3 m^3 d^{-1} per well).
- Methane emission due to diffusive flux is comparable to the most significant operational emissions (i.e., flowback).

GRAPHICAL ABSTRACT

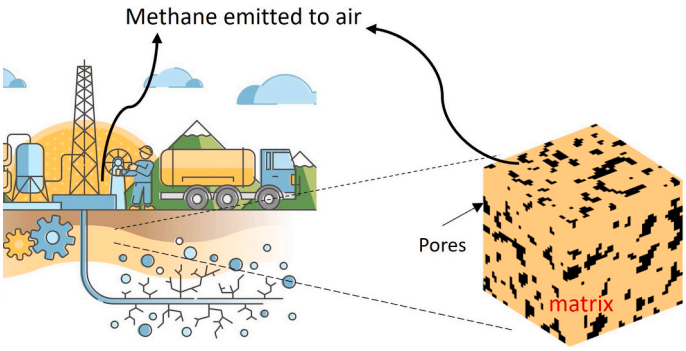

ARTICLE INFO

Editor: Pavlos Kassomenos

Keywords:
Natural gas
Methane emissions
Knudsen diffusion
Shale gas production

ABSTRACT

Shale gas, with its abundance and lower carbon footprint compared to other fossil fuels, is an important bridge fuel in the ongoing energy transition. However, a notable concern in shale gas exploration is fugitive methane emissions during the extraction, development, and transport of natural gas. While most existing works evaluate methane emissions released by well fracking, completion and operation, the greenhouse footprint of unproductive shale gas wells (often abandoned or orphaned) has received little scrutiny. A large fraction of these emissions from abandoned shale gas wells are due to the diffusive transport of methane trapped in nanoporous shale matrix, which is poorly understood. Here, we develop a theoretical kinetic approach to predict methane diffusive flux from heterogeneous shale matrix. Our theoretical model is based on a layer sequence formulation and accurately considers multiple flow mechanisms, including viscous flow, gas slippage, and Knudsen diffusion and their mutual interactions. The model is validated against the observed methane diffusion data obtained from high-pressure and high-temperature experimental measurements on Marcellus shale. We find that methane diffusive flux increases as reservoir pressure decreases. We estimate methane emission due to diffusive transport up to 20 × 10^3 m^3 per well per day, which is comparable to emissions from flowback fluid. For the first time, unrecovered natural gas in the shale matrix is demonstrated to be the main source of methane emissions from abandoned shale gas wells. Given the long-lasting nature of diffusive transport to shale gas seepage, it is suggested that regulatory requirements should be implemented to provide long-term monitoring of methane emissions from abandoned shale gas wells.

* Corresponding author.
E-mail address: szl3@psu.edu (S. Liu).

https://doi.org/10.1016/j.scitotenv.2023.169750
Received 27 October 2023; Received in revised form 24 December 2023; Accepted 26 December 2023
Available online 30 December 2023

1. Introduction

Methane contributes to a third of net warming since the Industrial Revolution with a much stronger global warming potential than carbon dioxide by 84–86 times over a 20-year timeframe (Myhre et al., 2013; IEA, 2023). Under the Global Methane Pledge, the U.S. and other partner countries have committed to reducing global methane emissions by ~30 % by 2030, highlighting the urgency of methane mitigation (IPCC, 2022). A significant source of methane inventory is abandoned oil and gas wells, contributing to 10 % of total methane emissions in the U.S. (EPA, 2023; Kang et al., 2014; Kang et al., 2016). Recent measurements (EPA, 2023; Boutot et al., 2022) suggest that the Appalachian basin has the highest number of abandoned wells, causing it becoming the largest source of methane emissions from such wells in the U.S. After well abandonment, fugitive emissions continue at the well site, where abandoned wells are likely to act as potential contamination pathways to atmosphere and groundwater aquifers (if unplugged or well integrity is compromised) (Kang et al., 2014; Boutot et al., 2022; Nisbet et al., 2020). Nevertheless, assessing methane emissions from abandoned wells is faced with substantial uncertainty because of poorly documented well records or the limited direct measurements available (Kang et al., 2023). It is therefore important to identify the mechanisms that lead to high emissions and develop predictive modeling to estimate methane flow rate over time.

In the Appalachian basin, Marcellus shale formation is the largest natural gas production formation, making it the primary contributor to methane emissions in the basin (Caulton et al., 2014). Methane emissions from shale gas development can account for up to 12 % of lifetime production, which includes emissions both upstream at wellsite and midstream during processing (Pétron et al., 2012; Karion et al., 2013). Existing efforts (Pétron et al., 2012; Karion et al., 2013; Howarth et al., 2011) to assess emissions from shale gas production are mostly constrained to the operating life of these wells. An important missing source is abandoned shale gas wells. The most unique characteristics of shale gas wells is the low recovery factor (mostly <20 % (Neil et al., 2020; Ma et al., 2022)), leaving significant amount of gas reserves unrecovered following well abandonment. The remaining gas reserve primarily resides in nanopores of shale matrix, where concentration-driven diffusion drives the migration of methane molecules (Chandra et al., 2020; Clarkson et al., 2013). Contrary to the pressure-driven advection flow of natural gas, which terminates when the reservoir is depleted, diffusion is a slower, passive transport process. It contributes to a long-lasting methane flow flux that continues after well abandonment. As a result, we often observe a transient nature in methane leaks from shale gas wells (Caulton et al., 2014) as well as underground coal mine (Singh et al., 2022; Kholod et al., 2020; Vishal et al., 2013). Here, we focus on the mechanistic understanding of emission mechanisms in abandoned shale gas wells.

As noted earlier, the remaining gas reserve in abandoned shale gas wells primarily resides in shale matrix, consisting of nanoporous pore network. To characterize abandoned shale gas well's potential as a methane emission source, a solid understanding of shale gas transport mechanism is required. Fig. 1 shows typical production profile in major U.S. shale plays. The initial high gas production rate sources from depleting interconnected natural and hydraulic fractures, where the slope of the decline curve is proportional to $\sqrt{t}$; later in the production profile, an asymptote in production presents and lasts for many years at a flat or slowly declining rate, known as elongated tail production (Patzek et al., 2013; Middleton et al., 2015). This production tail is of direct relevance to evaluate methane flow flux after well abandonment. While the early-time regime, mainly fed by gas stored in fracture network as free compressed gas, is well depicted by the classic Darcy formulation, the late-time regime, mainly fed by gas stored in nanoporous matrix as free and adsorbed gas, poses a distinctive challenge in gas flow modeling. Since pore throat size of shale is comparable to the mean free path of gas molecules (Clarkson et al., 2013), gas diffusion dominates matrix transport. As a result, diffusion is the most important flow mechanism for highly depleted abandoned wells with low reservoir pressures. It should be noted that shale matrix typically has a wide pore size distribution, and multiple flow mechanisms can come into play, affecting each other. Therefore, it is important to develop a fundamental understanding of multi-scale flow mechanisms underlying shale matrix transport so that methane emission potential from abandoned wells can be properly estimated. There are many approaches in modeling gas transport in nanoporous shale matrix. Molecular dynamics (MD) models have successfully predicted the transport rate of pure and mixed gas in nanoporous media (Dubbeldam and Snurr, 2007). But it requires a multitude of properties pertaining to the nanopore system and thus, is computationally too intensive for physically and chemically heterogeneous shale, even with simple fluids. As a result, the search for a tractable theory based on molecular theory is of much practical value and significance. Drawing from this premise, most models (Wu et al., 2015; Javadpour, 2009; Darabi et al., 2012; Azom and Javadpour, 2012; Klinkenberg, 1941; Ertekin et al., 1986) developed for practical applications consider the superposition of diffusive and viscous resistance following the dusty gas model formulation (Mason and Malinauskas, 1983; Evans III et al., 1961). The viscous part is derived by modifying Poiseuille flow model for a non-slip boundary at pore surface, whereas the diffusive part superimposes Knudsen and molecular diffusion coefficients. However, there is no consistency for the superimposing rule (weighing factor corresponding to individual flow regime). For example, the Klinkenberg approach (Klinkenberg, 1941) neglects the contribution of Knudsen flow to the total flow rate, whereas the work of Ertekin et al. (1986) excludes slip flow from the formulation.

In brief, practical models quickly estimate matrix permeability but can be inaccurate. MD gives precise permeability estimates but is limited to small systems over short periods. As a result, a simplified pore structure model is often surmised in predicting matrix transport. To the best of our knowledge, no study attempts to predict the observed shale gas permeation involving complex pore structure framework due to a lack of mechanistic understanding of the interactions between different flow regimes.

In this work, we propose an analytical model to estimate methane emission potential of abandoned shale gas wells, focusing on the

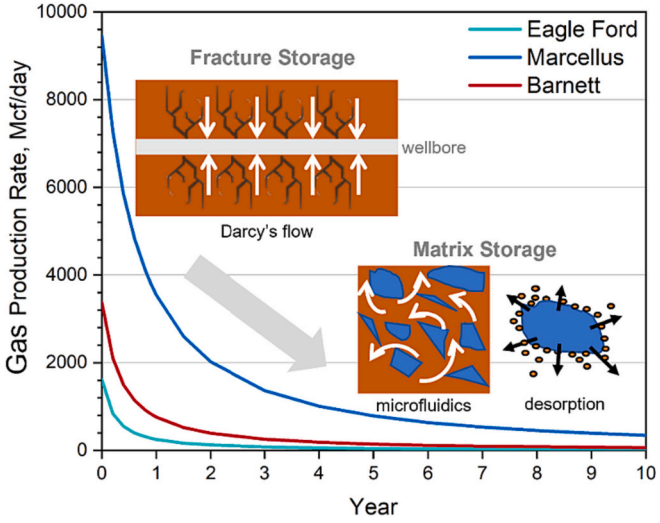

Fig. 1. Field-level shale gas production curve (obtained from major U.S. shale plays) depicting the dominant flow mechanism governing gas transport. Various matrix flow regimes (e.g., slip flow, Knudsen diffusion) are likely to occur in long-term tail production that dominates the total shale gas production.
Data source: EIA (2022).

remaining gas reserve in shale matrix. Specifically, a unified gas transport model is developed based on theoretical framework of kinetic theory to describe confined fluid behavior in nanoporous shale matrix. The rest of the paper is structured as follows. Section 2 develops a unified gas transport model to predict flow flux as a function of pore structure parameters and reservoir pressures. The conceptual model is a layer-by-layer sequence model considering interactions between various flow mechanisms. Section 3 provides a detailed overview of experimental work involved in high pressure and high temperature matrix flow measurements. Section 4 contributes to model validation and application. The proposed model is validated by experimental measurements on shale matrix transport and later applied to predict diffusive flow flux as a function of pressure and estimate methane emission potential for abandoned shale gas wells.

2. Theory of gas flow through nanoporous shale

Gas transport in the porous matrices is bound to two asymptotic regimes, i.e., Knudsen diffusion (driven by molecule-wall interactions) in small pores and continuum/viscous/bulk flow (driven by molecule-molecule interactions) in large pores (Veldsink et al., 1995). A distinct transport coefficient prevails in each of these regimes. Assuming mutual independence of molecule-wall and intermolecular interactions permits the applicability of the Bosanquet formula (Bosanquet, 1944; Mistler et al., 1970; Yang and Liu, 2019) to estimate the overall transport coefficient in the transition region. Bosanquet formula (Eq. (1)) combines molecule-wall and molecule-molecule interactions to calculate self-diffusivity of specific species in one dimension. Mathematically,

$$\frac{1}{k_t} = \frac{1}{k_k} + \frac{1}{k_v} \tag{1}$$

where k_t, k_k, k_v are effective permeability corresponding to flow under transitional, pure Knudsen, and pure viscous flow regimes, respectively.

This approximation that postulates the additivity of the two collision frequencies is accurate in the absence of any interdependence between wall and intermolecular collisions (Goodbody et al., 1991). If intermolecular collisions are strongly correlated with wall collisions which is the rarefaction effect, Bosanquet's formula no longer applies, and gas kinetic theory should be revisited to account for wall surface effects adequately. A layer-sequence model first proposed by Bravo (2007) is therein applied to lump the molecular effects into a space-averaged macroscopic flow property (Fig. 2). In adjacent to the pore wall, surface effects are prevalent and correspondingly, molecule-wall collisions become the primary driving force for gas transport. This layer is commonly known as the Knudsen layer where collisions among molecules are neglected in the formulation for Klinkenberg's equation (Klinkenberg, 1941). This is indeed valid for slip flow regime where molecular mean free path, λ is comparably smaller than the length scale of the pore network, *d*, but tends to be erroneous as the characteristic scale further decreases, corresponding to transitional flow region. In engineering practice, a wide span of pressure range can be encountered during depletion and injection that brings in scale-wide changes in collisional frequencies. So, both intermolecular and wall collisions may play comparable roles for in-situ gas flow through a cascade of smaller voids and hierarchical pore structure. Based on the formalisms of the dusty gas model, the following work is dedicated to developing a generalized and unified transport model to provide a complete solution to the in-situ gas transport problem from the viscous to molecular regimes. Correlations between successive molecule-wall and intermolecular collisions will be considered within the Knudsen layer and in the central zone of pores.

As shown in Fig. 2, gas flow through a simplified and straight capillary tube, the assumed pore shape, is hypothetically separated into viscous stream in the inner section (middle layer) surrounded by Knudsen layers in the outer annulus (upper and lower layers). In viscous stream, only molecule-molecule interactions occur; in Knudsen layers, both molecule-molecule interactions and molecule-wall interactions. At the high-pressure upstream, gas molecules have more frequent intermolecular collisions than pore wall collisions, leading to the formation of a thicker viscous stream layer relative to the Knudsen layer. At lower pressures, pore wall collisions become more pronounced as more gas molecules collide with the pore wall, resulting in an increased thickness in the Knudsen layer. This postulation does not imply an independent layer-sequence transport process. In fact, gas transport in different flow streams is mutually affected as molecules leave, join, and rejoin the stream, which has not yet been adequately considered.

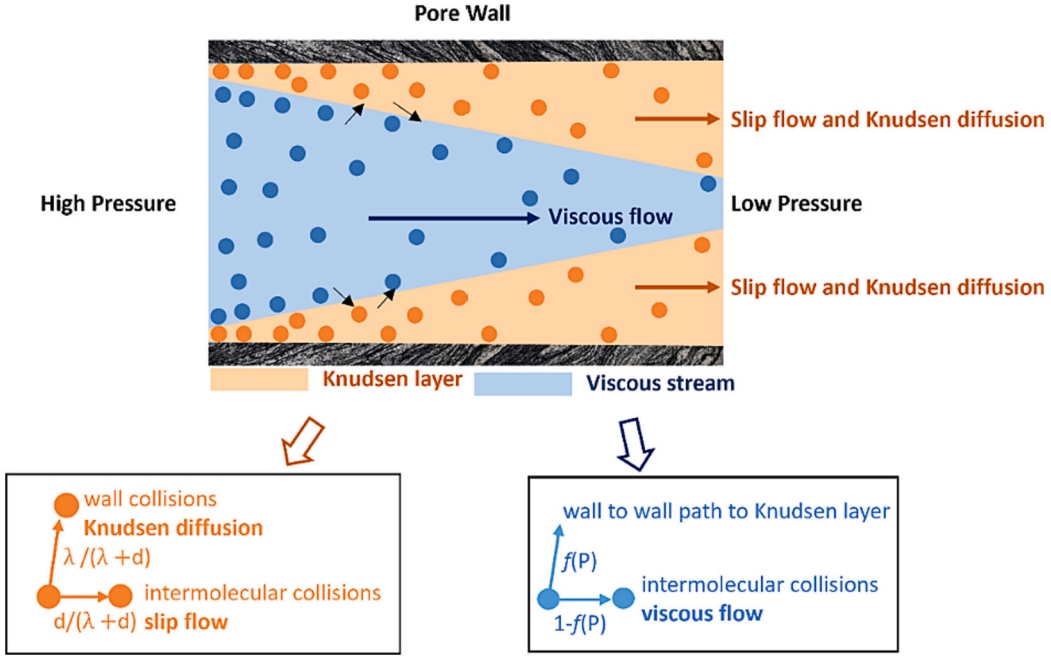

Fig. 2. Multi-mechanism gas transport through nanopores of shale matrix. *f(P)* is the fraction of gas molecules leaving the viscous stream.

2.1. Flow equation in viscous stream

In the inner flow path of the capillary, molecule-molecule interactions and the resulting dissipative viscous forces primarily drive gas transport in the viscous stream, whereas wall effects only act on the outer annulus. The gas flux can be defined by Hagen-Poiseuille equation following (Eq. (2)) (Hagen, 1839; Bird and Stewart Warren, 2007).

$$q_v = -\frac{\pi d^4}{128\mu}\frac{dP}{dL} \tag{2}$$

where q_v is the volumetric gas rate, d is the pore diameter, $\frac{dP}{dL}$ is the pressure gradient, and μ is the gas viscosity.

A fraction of gas molecules may leave the viscous stream due to the engagement of wall-to-wall path (Fig. 2). Considering this interplay between inner and outer regions, a correction factor, $f(P)$ is added to Eq. (2) to allow for the transmission of kinetic energy produced by the pressure gradient to tube wall. Gas viscosity, μ can be related to mean free path, λ by (Eq. (3)) (Vincenti and Kruger, 1965).

$$\lambda = \frac{\mu}{P}\left(\frac{\pi RT}{2M}\right)^{\frac{1}{2}} \tag{3}$$

and the resulting viscous flow equation can be expressed as (Eq. (4)),

$$q_v = -\frac{\pi d^4}{128\lambda P}\left(\frac{\pi RT}{2M}\right)^{\frac{1}{2}}(1-f(P))\frac{dP}{dL} \tag{4}$$

where $f(P) = e^{-sinh^{-1}\left(\frac{1}{Kn}\right)}$, as suggested by Scott and Dullien (Scott and Dullien, 1962), T is the absolute temperature, M is the molecular weight of gas, and R is the gas constant.

2.2. Flow equation in Knudsen layer

In microscale gas flow, the small dimension of capillary tubes means that the flows are often rarefied. Flow behavior near the solid bounding surfaces is governed by molecule-wall interactions, leading to the formulation of the Knudsen layer. This layer is a local thermodynamically nonequilibrium region extending a few mean free paths from the surface (Dongari et al., 2011). Considering the transitional flow regime where both molecule-wall and molecule-molecule collisions are comparably important towards the gas flux, slip flow and Knudsen diffusion are very likely to coexist in gas transport within Knudsen layer. Previous gas transport models, such as Klinkenberg's equation (Klinkenberg, 1941; Heller et al., 2014) or weighted-average model (Ertekin et al., 1986; Liu et al., 2002) integrate either slip flow or Knudsen diffusion into the continuum flow equation and ignore the other flow regime. To fill this gap, Javadpour's model (Javadpour, 2009) and its extensions (Wu et al., 2015; Javadpour et al., 2012; Civan et al., 2012) integrate Knudsen diffusion into Klingenberg's equation to improve predictions on the slip velocity comprising of the streaming velocity of incident molecules and that of the scattered molecules. This approximation asserts the linear additivity of flow flux through slip flow and Knudsen diffusion and should be very accurate in the absence of any interaction between intermolecular and wall collisions. A more general formulation that extends Klinkenberg's equation and describes detailed different molecule interactions at pore scale in terms of kinetic theory is developed as follows.

Assuming the validity of Knudsen diffusion implies straight trajectories between collisions at opposite pore walls such that no correlations exist between successive wall collisions. In reality, molecules that are reflected on the pore wall are likely to collide with other molecules prior to another wall collision, whereby the frequency of intermolecular collisions is controlled by pressure gradient. This phenomenon results in the occurrence of slip flow. As a means of evaluating the interactions between the two flow regimes, Maxwell-Boltzmann distribution (Maxwell, 1965) (the chi distribution of speeds of gas molecules at a certain temperature) is used to calculate the likelihood of wall collisions and intermolecular collisions among a unit volume of gas molecules. This classical distribution describes the velocities of idealized gas molecules in a system at thermodynamic equilibrium.

The total number of molecules impinging upon per unit length of wall per unit time, N_{wall} is given by (Eq. (5)) (Maxwell, 1965).

$$N_{wall} = \frac{1}{4}n\bar{c}\pi d \tag{5}$$

where n is the molar density and $\bar{c}$ is the mean molecular velocity.

The total number of intermolecular collisions per unit length of wall per unit time, $N_{molecule}$ is given by (Eq. (6)) (Maxwell, 1965).

$$N_{molecule} = \frac{1}{4}\frac{n\bar{c}}{\lambda}\pi d^2 \tag{6}$$

Therefore, at any time, the possibility of wall collisions over total collisions, f_{wall} is given by (Eq. (7))

$$f_{wall} = \frac{N_{wall}}{N_{wall}+N_{molecule}} = \frac{\lambda}{d+\lambda} \tag{7}$$

This ratio is useful in evaluating the interaction between slip flow and Knudsen diffusion, which describes the contribution of molecule-molecule collisions to flow flux in Knudsen layer. When gas molecules impinge on the walls, part of them undergo diffusive reflection and subsequently collide with other molecules from upstream, known as first-order slip (Beskok and Karniadakis, 1999). The rest of gas molecules experience specular reflection and thereafter, either participate in the wall-to-wall path (Knudsen diffusion) or join the fluid streams (slip flow), leading to correlations between successive molecule-wall collisions. To quantify this correlation, we use f_{wall} to approximate the possibility of these perfectly reflected molecules involved in pure Knudsen diffusion (and not affected by intermolecular collisions).

A usual calculation of slip velocity is a simplified case that only considers first-order gas slip or tangential momentum exchange of gas molecules at the surface (Eq. (8)) (Beskok and Karniadakis, 1999; Kennard, 1938; Thompson and Owens, 1975),

$$u_s - u_w = \frac{2-\sigma_v}{\sigma_v}\lambda\left(\frac{\partial u}{\partial n}\right)_{wall} \tag{8}$$

where u_s and u_w are the slip and wall velocity, respectively. σ_v is the tangential momentum accommodation coefficient measuring the fraction of gas molecules undergoing diffusive reflection over specular reflection (Maxwell, 1965). n is the coordinate normal to the wall.

Considering the influx of gas molecules coming from perfect reflection, the flow rate of slip flow, q_s can be derived as (Eq. (9)),

$$q_s = -\frac{\pi}{12}\frac{d^3}{P}\left(\frac{\pi RT}{2M}\right)^{\frac{1}{2}}\left(\frac{2-\sigma_v}{\sigma_v}+(1-f_{wall})\right)\frac{dP}{dL} \tag{9}$$

Theoretical analysis often ignores the second term representing the part of flow flux due to specular reflection to the pressure-driven stream. This is indeed applicable for cases with very small or very large Knudsen numbers, resulting $f_{wall}\rightarrow 1$. Here, we develop a general formulation for slip flow calculation, which improves predictions for transitional flow with intermediate Knudsen number ($0.1 < Kn < 10$).

For gas molecules exclusively involved in wall-to-wall path, the calculation of flow rate that postulates Knudsen model, q_k is given by (Eq. (10)) (Jeans, 1921).

$$q_k = -\frac{1}{3}\frac{d^3}{P}\left(\frac{\pi RT}{2M}\right)^{\frac{1}{2}}f_{wall}\frac{dP}{dL} \tag{10}$$

2.3. Integration of mass transfer for multiscale and multimechanistical flows

Multiscale gas transport phenomena are ubiquitous in gas perme-

ation in tight geologic media due to the wide span in operating conditions (pressure and temperature) or pore size distribution within the host rocks. A unified gas transport model is developed on the basis of viscous flow, slip flow, and Knudsen diffusion to quantify the multiscale flow behavior for microporous materials. The total flux is given as,

$$q_t(d) = q_v + q_s + q_k \tag{11}$$

Eq. (11) is the unified gas transport model developed for flow through microchannels with a uniform cross section. For natural rocks, a wide pore size distribution (PSD) is prevailing, necessitating further investigations to quantify the overall impact of porosity fluctuations on gas transport.

2.4. Mass transfer in the shale matrix pore structure

Without losing the generality, a parallel pore model depicted in Fig. 3 is conceptualized to extend the unified model (Eq. (11)) for heterogenous microporous media (e.g., shale matrix). The hierarchical pore network of a shale matrix is conceptualized and geometrically idealized into a bundle of capillaries with various radii, assuming cylindrical-shaped and interconnected pores. To incorporate local features at pore-scale into macroscopic flow formulations, we do not attempt to differentiate pore throat size from pore body size; instead, a smooth surface is assumed for nontrivial development. In cases of gas production or acid gas injection, layers of adsorbed gas molecules on the surface tend to hide real surface features and alleviate associated effects on bulk gas transport (Yang and Liu, 2020). As a result, impacts of surface heterogeneity can be ignored in the calculation of macroscopic gas velocity when surface diffusion (movement of adsorbed molecules) is significant. It is worthwhile to mention that the current model can be extended to incorporate these localized feature by coupling features into Knudsen model (Yang and Liu, 2019; Kärger et al., 2012).

Flow flux for a rigid pore channel is readily quantified from the unified model developed (Eq. (11)). For a range of pore sizes, the overall flow flux is quantified as the net sum of mass transported through every capillary contained. The mathematical expression of q_t for heterogeneous porous material is given as follows (Eq. (12)):

$$q_t = \int_{x_{min}}^{x_{max}} q_t(d)\rho(d)dx \tag{12}$$

where x_{max} and x_{min} define the upper and lower bound for every possible pore size present, as delineated by N_2-adsorption-derived PSD. Gas flux through single-sized pores, $q_t(d)$ is determined from Eq. (11) and its volume fraction is denoted by $\rho(d)$.

3. Experimental work

3.1. Sample information

The Marcellus shale investigated was obtained from the Pennsylvania Department of Conservation and Natural Resources (PA DCNR), Bureau of Topographic and Geologic Survey (BTGS) core library located in Middletown, Pennsylvania. The shale sample is obtained from Eastern Gas Shales Project (EGSP) collected cores. This shale is located in the western half of the Appalachian basin (Marcellus formation), containing a large natural gas reserve but very low permeability (Dyman and Wilcox, 1983; Schmoker, 1980). Based on reported gas permeation measurements, the permeability of Devonian-age Marcellus shale varies greatly, ranging from $<0.2\times10^{-8}$ to 0.8 md (Luffel et al., 1993). In this

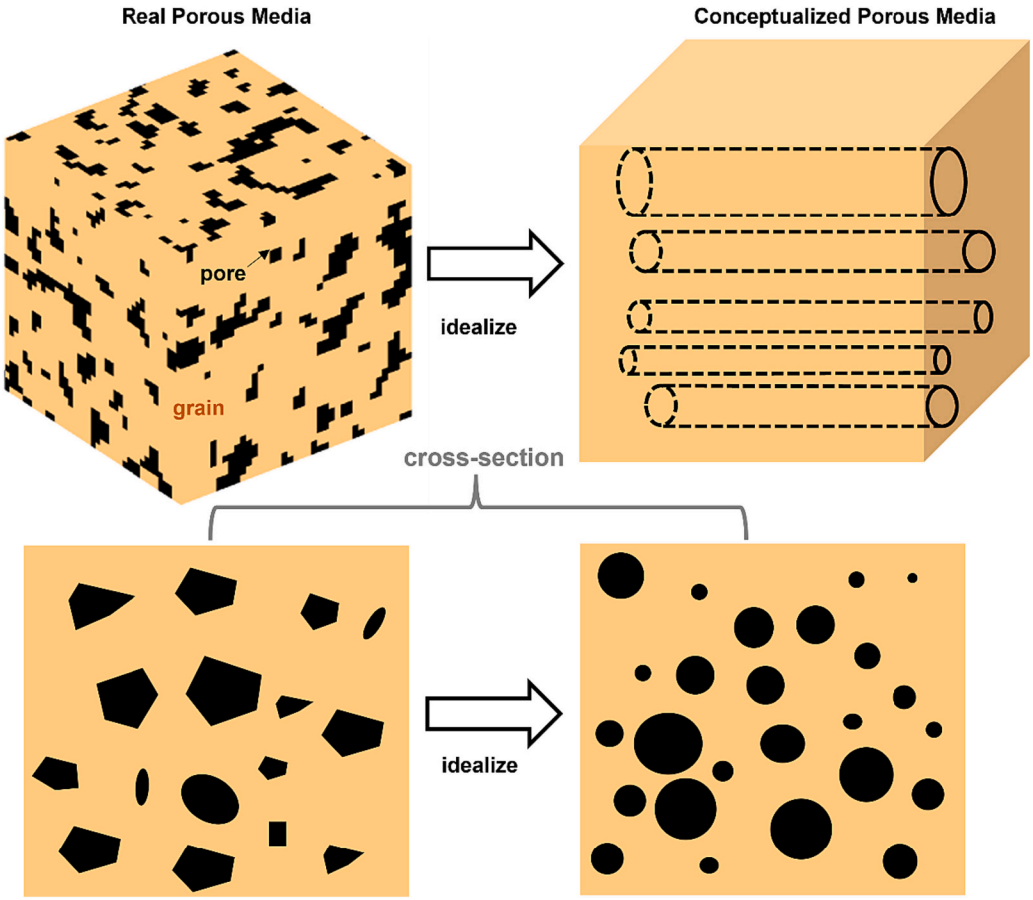

Fig. 3. Conceptual model of heterogenous porous media (e.g., shale matrix). The porous medium is represented by a capillary bundle model comprising a collection of tubes with a variable cross-sectional area.

work, a crushed shale sample was prepared by manual grounding and sieving to avoid over-gridding and to ensure sufficient sample mass can be recovered at the target grain size (~70 mesh). The pore volume and its size distribution were determined from the nitrogen adsorption experiment at 77 K using ASAP 2420 Automated Surface Area and Porosimetry System. According to Barret, Joyner, and Halenda (BJH) (Barrett et al., 1951) approximation, the Marcellus EGSP shale has a bimodal pore size distribution with a significant fraction distributed in pores with a size <10 nm (Fig. 4).

3.2. Experimental apparatus and method

The apparatus for measuring high-pressure gas adsorption kinetics is described elsewhere (Yang et al., 2022). Characterization of adsorption equilibrium has been in the previous work, and this work focuses on the quantification of diffusion and transport of confined fluids in a nanoporous shale matrix.

Matrix permeability of shale is generally very low and, thus, challenging to be accurately measured. Because of the extensive time required to achieve equilibrium, permeability measurements following the steady-state method do not apply to shale matrix (Cui et al., 2009). As a transient method, the pulse-decay technique is commonly employed for permeability measurements on tight rocks, where its elapsed time is only about minutes to hours for ultra-low permeability rocks (~10^{-12} md) (Brace et al., 1968; Trimmer et al., 1980; Yamada and Jones, 1980). The pulse-decay method can potentially overestimate of matrix permeability due to the coring-induced microfractures and the effect of natural fractures. To avoid this artifact, the crushed sample was used that could eliminate fractures completely and ensure gas flow purely through the nanoporous network of shale matrix (Egermann et al., 2005).

The methane adsorption and diffusion measurements were conducted on the custom-built volumetric differential pressure apparatus, as shown in Fig. 5. A differential pressure transducer with an operating range of ±50 psi (0.34 MPa) was deployed to continuously monitor pressure drops due to adsorption and diffusion, offering a significant increase in accuracy as compared to Sieverts apparatus (up to 10-fold) (Yang et al., 2022). The testing system operates on the basis of symmetrical seating of void volume and consists of two symmetrical Sieverts apparatus. Accordingly, gas permeance measurements were initiated by injecting methane into the outer loop (cells and tubing outside the inner valves) to the desired pre-expansion pressure and then connecting the outer with the inner loop (cells and tubing inside the inner valves) to achieve equilibrium conditions. A cumulative injection scheme was deployed, where transient pressure data collected at different pressure stages delineated the experimental relationship between matrix transport capacity and pressure. The pressurization procedure was repeated with an equilibrium pressure ranging from 2 to 14 MPa at an isothermal condition of 303.15 K.

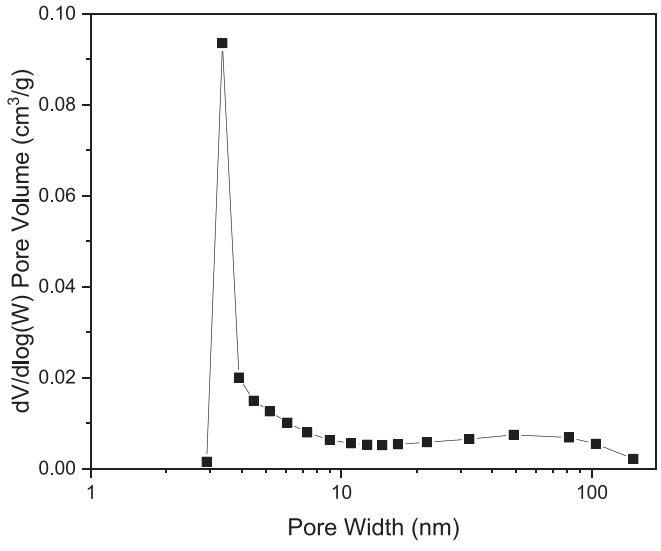

Fig. 4. Pore size distribution of the studied EGSP shale obtained from the low-pressure nitrogen adsorption data (77 K).

As gas molecules penetrate through nanopores, ambient pressure in the sample cell gradually decreases, accompanied by an increase in differential pressure readings (see Fig. 6). Gas flow flux was estimated using the pulse-decay pressure data collected as follows (Eq. (13)):

$$F(t) = \frac{1}{RT}(V_{ss} - V_s)\left(\frac{\Delta P(t)}{Z_s} - \frac{\Delta P_e}{Z_e}\right) \tag{13}$$

where $F(t)$ is the mole fraction of gas molecules flowing into the nanopores (normalized by the adsorption equilibrium value), $V_{ss} - V_s$ is the void volume in sample cell, $\Delta P(t)$ is transient differential pressure readings, ΔP_e is the equilibrium differential pressure, and Z_s and Z_e are gas compressibility factors corresponding to transient and equilibrium pressures.

As shown in Fig. 6, the magnitude of measured pressure drop (<0.005 MPa) at each pressure stage was about the same or even less than the precision of a typical absolute pressure transducer (with a measuring scale of 35 MPa) (Yang et al., 2022). Clearly, the absolute pressure transducer as well as the conventional volumetric method cannot meet the accuracy required for characterizing shale gas transport with comparatively low adsorption capacity (concerning coal). The improved differential volumetric method using differential pressure transducer can significantly reduce the systematic error at high line pressure measurement, therefore offering the precise measurement for gas diffusivity. A detailed discussion on the improved differential volumetric method is discussed in our previous work (Yang et al., 2022).

4. Model validation and application

The unified gas transport model was first tested on synthetically manmade material and then on natural material because the matrix pore structure of tight rocks is convoluted and is of less confidence (Clarkson et al., 2013). In addition, evaluating overall gas permeation for adsorbing gas requires separating the contribution of surface diffusion from the free gas flow, which challenges the present model and necessitates using a suitable adsorption model to predict the thermodynamic equilibria. This involves further modifications to the current model on the basis of the weighted superposition of bulk and adsorbed gas transport fluxes, which is discussed later. Therefore, model validation will root on the experimental measurements of inert gas (such as argon and helium) transport in the synthetic material as a reference for ideal conditions with adsorption- and bumps-free surface and extend to real conditions accounting for adsorption and surface roughness associated with shale matrix.

4.1. Validation of gas transport model in homogenous and heterogenous nanoporous membrane

The proposed unified gas transport model was applied to predict gas transport behavior in artificial membranes with a pore size gradient from 0.5 nm to 212 nm for testing its general applicability to the multiscale flow behavior. A comparison between proposed model estimation and experimental data reported for inert gas transport in these membranes (Roy et al., 2003; Katsaros et al., 1997) is conducted in this model validation section. The reported nanopore flow data was collected on alumina filters with uniform pore size and carbon membranes with right-skewed normal pore size distribution (see Fig. 7). Table 1 lists the dimension of nanopores involved and the physical properties of flowing fluid.

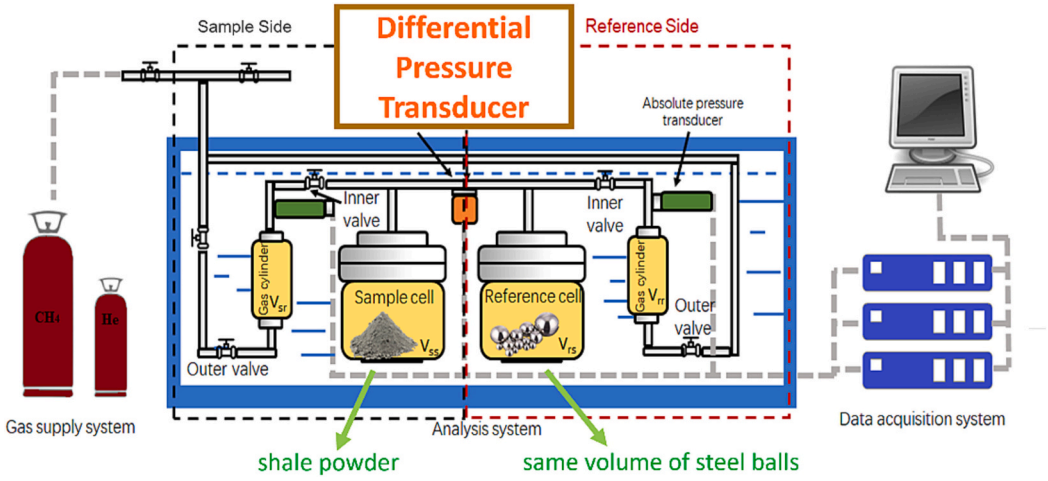

Fig. 5. Schematic of the volumetric differential adsorption apparatus. V_{sr} and V_{rr} denote charging cells at the sample and reference sides. V_{ss} and V_{rs} denote sample cells at the sample and reference sides.
Modified from (Yang et al., 2022).

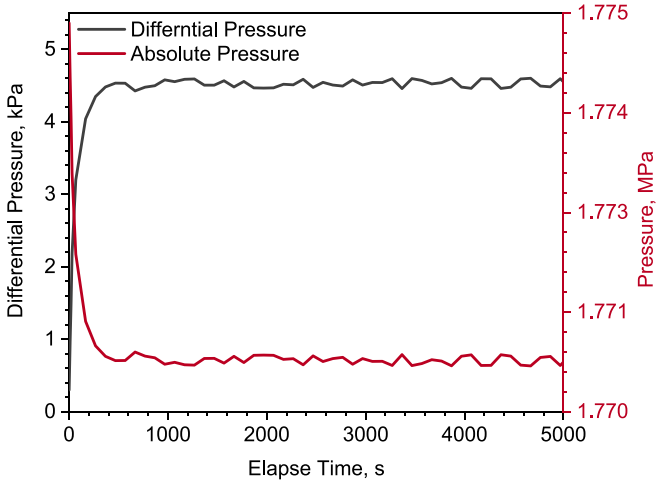

Fig. 6. An example of measured absolute and differential pressure changes during CH_4 permeation into the nanoporous network of shale matrix.

We used Eq. (11) to calculate the flow flux in these membranes with well-defined pore shape and pore size distribution. Our model can accurately replicate the flow behavior for Argon transport in alumina filters as a homogenous porous material with an average error of 4.5 % (Fig. 8, top). To achieve this match, the associated value for the tangential accommodation coefficient, σ_v, was found to be 4/3,

Table 1
Pore dimensions and gas properties.

Flow parameter	Alumina filters (Roy et al., 2003)	Carbon membranes (Katsaros et al., 1997)
Pore size distribution	Discrete, single value	Right-skewed normal
Mean pore diameter, *d*	212 nm	0.8 nm
Length, *L*	60 μm	15 nm
Temperature, *T*	300 K	310 K
Pressure difference	Vacuum to 120 kPa	100 kPa
Outlet pressure, P_{out}	4.8 kPa	35 to 425 kPa
Gas species	Argon	Helium
Molecular mass, *M*	39.948 g/gmole	4.003 g/gmole

consistent with Maxwell's work (Maxwell, 1965). When applied to heterogenous porous materials (carbon membranes), Eq. (11) was integrated over the reported pore size distribution from 0.5 to 1.5 nm following the algorithm depicted in Eq. (12). The unified transport model is developed based on the conceptual model of capillary bundles, where mutual interactions between pores in different sizes were ignored. Under this assumption, linear additivity for flow flux in different-sized pores was employed to calculate the overall mass flow flux for the heterogeneous membrane. The modeling results reasonably match experimental data with an average error of 9.1 % (Fig. 8, bottom). This supports the rationale behind the capillary bundle model and validates the use of linear additivity for modeling gas transport in heterogenous porous media with a range of pore sizes. Note that gas

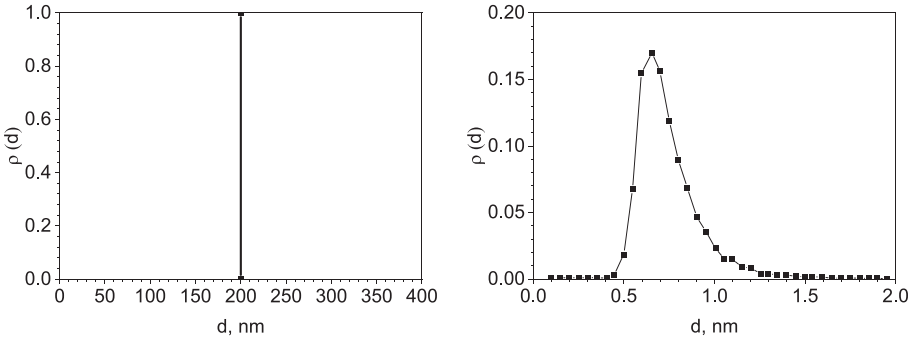

Fig. 7. Pore size distributions based on nitrogen adsorption for homogenous nanoporous material, alumina filters (left) and heterogenous nanoporous material, carbon membrane (right) (Roy et al., 2003; Katsaros et al., 1997). Note that *(d)* is determined from the reported pore volume data normalized to total pore volume.

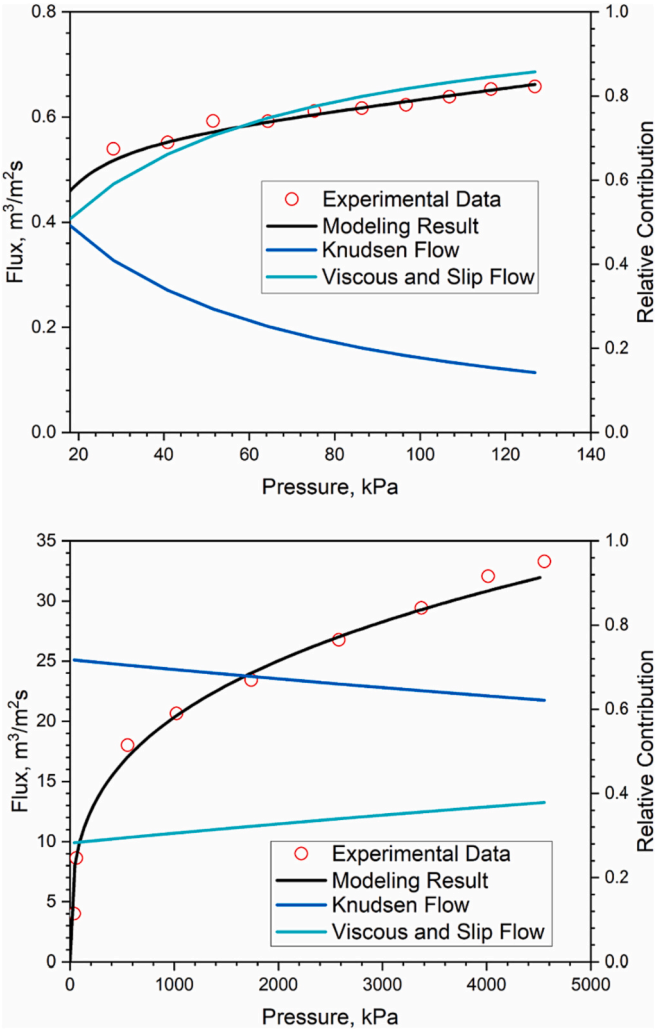

Fig. 8. Applying the unified transport model (Eq. (11)) to experimental data for inert gas transport in synthetic alumina filters and carbon membranes. The relative contributions of Knudsen diffusion and corrected viscous flow (slip and pure viscous flow) to total gas flow are also plotted as scaled by the right y-axis.

permeance (m^3/m^2 s kPa), a ratio of flow flux over the thickness of membrane per unit driving force, was used in the original work (Katsaros et al., 1997) to characterize the flow conductance of carbon membranes. Herein, it was converted to volumetric flow flux (m^3/m^2 s) for unit consistency for model validation. By comparing modeled results against the experimental data, our model is widely applicable to both homogenous and heterogeneous manufactured nanoporous material, suggesting the importance of considering the interactions among different flow regimes (viscous, slip, and Knudsen flow).

In Fig. 8, the interaction between corrected viscous flow (pure viscous and slip flow) and Knudsen diffusion was characterized by the relative contribution of mass transfer under a single flow regime to the total mass transported. At pressures investigated, flow in macroporous alumina filters with a uniform pore size (~212 nm) belongs to transitional flow with Knudsen number ranging from 0.3 to 3. In this case, the molecular mean free path is generally comparable to the characteristic dimension of the solid, and thus, molecules present in the viscous stream are very likely to interact with pore walls. A calculation of *f (P)* indicates that up to 60 % of gas molecules following intermolecular collisions are constrained by pore walls, and this interaction is diminishing at higher pressures. As such, the flux ratio contributed by Knudsen diffusion is inversely related to pore pressures. At the highest pressure reached, the corrected viscous flow contributes to ~85 % of total mass transfer. If the interactions between diffusive and advective flux (characterized by *f (P)*) are overlooked, the flow conductance at reported pressures would be greatly overestimated due to the underrating Knudsen layer effects.

Similar observations were made for the heterogenous microporous carbon membrane, where the net flux through Knudsen diffusion decreases as pressure increases. The carbon membrane examined here features persistent pores <2 nm in diameter. Herein, molecule-wall collisions dominate overall gas transport, contributing to >60 % of mass transport (Fig. 8, bottom). Gas permeation in this microporous material evolves from a simple Knudsen diffusion to a more complex transitional flow regime with increasing pressures. Since the dominant pore size (~0.8 nm) is much smaller than the molecular mean free path at investigated pressure ranges (5 to 600 nm), a calculation of f_{wall} yields a value very close to one, implying the predominance of Knudsen layer. Still, a small fraction of reflected gas molecules (1-f_{wall}) is likely to be hit by upstream molecules before another wall collision. As pressure increases, the interplay between different flow mechanisms becomes increasingly significant, as evidenced by the convergence of the two lines representing the relative contribution. Increasing the pressure increases the likelihood of intermolecular collisions, which in turn decreases the proportion of gas molecules involved in wall-to-wall motion and increases the contribution of slip flow.

Overall, interactions between various flow regimes exhibit strong dependence on pore pressure. For microporous media (carbon membrane), intense interactions between diffusive and advective fluxes occur at high pressure stages; for macroporous media (alumina filters), the opposite trend is found where the interactions become trivial towards high pressures. In this section, it is demonstrated that the general applicability of the proposed model in artificial nanoporous material with well-defined pore architecture. The heterogeneity considered here is only for unimodal PSD over a relatively narrow spectrum of values. Further investigations will be performed by comparing model's predictions with the experimental data measured on shale matrix.

4.2. Gas transport modeling and its validation in heterogeneous shale matrix

The data shown in Fig. 9 is the adsorption isotherm of CH_4 measured at 303.15 K for the studied EGSP shale sample (~48 g). The Langmuir isotherm was employed to describe the observed adsorption equilibria following least-squares minimization. The optimized Langmuir volume, characterizing the ultimate adsorption capacity, is estimated to be 0.05 mmol/g. Previous work (Yu et al., 2016) reported a range of adsorption

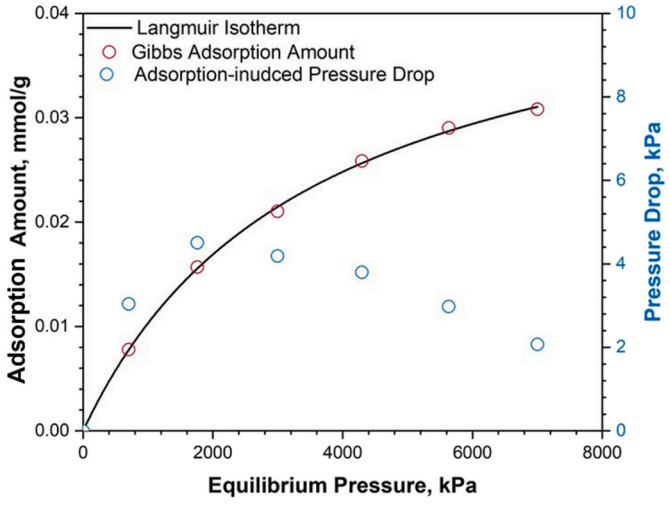

Fig. 9. The methane Gibbs adsorption isotherm at 303.15 K and the corresponding adsorption-induced pressure drops recorded using the differential volumetric apparatus. The solid line is Langmuir fit to adsorption data.

capacity for EGSP shales (with total organic content (TOC) ranging from 0.03 to 0.09) varying between 0.06 and 0.3 mmol/g. As our measured sample has a TOC content of 0.03, the measured adsorption capacity (~0.05 mmol/g) is consistent with literature-reported values, verifying the accuracy of the experimental results. According to data recording made by the differential pressure transducer, the pressure drop due to gas adsorption is only about 0.03 % to 0.4 % of the ambient pressure in the sampling cell, below the sensitivity of a conventional absolute pressure transducer (Yang et al., 2022). As many shale formations possess 1 to 5 % of organic material (Miller, 2015) corresponding to weakly adsorbing systems, the conventional volumetric method based on absolute pressure readings is prone to errors in quantifying the adsorption capacity, especially for shale samples with low TOC. Therefore, differential pressures were used to evaluate the adsorption capacity of the studied shale.

Note that the experimentally obtained adsorption isotherm shown in Fig. 9 consists of Gibbs surface excess quantity at equilibria as opposed to absolute adsorption volume. The excess adsorption volume measures the difference between the number of moles of gas present in the system and the number of moles that would be present if all the void volume in the system were taken by the adsorbate gas in its bulk phase at the same condition (Sudibandriyo et al., 2003). In other words, the changes in void volume in the system due to the condensation of adsorbed molecules are neglected in calculating the excess adsorption amount. It may seem attractive to consider the absolute adsorption isotherm, but estimating actual amounts adsorbed from the measured excess adsorption variables concerns making ambiguous assumptions about the size of the adsorbed phase. However, the volume and structure of the adsorbed phase as well as the actual density profiles of the adsorbate within the adsorbed phase, cannot be experimentally characterized (Sircar, 1999). From an engineering viewpoint, excess adsorption is more practical to represent the true experimental variable and circumvent the challenge of characterizing the adsorbed phase (Purewal et al., 2009).

The normalized adsorption kinetics curves of CH_4 at different pressure stages are shown in Fig. S1. In general, CH_4 adsorption reaches equilibrium in <600 s, and the associated elapse time increases as more gas adsorption sites become occupied at higher pressures. Beyond 3 MPa (close to Langmuir pressure of 3.5 MPa), the equilibrium time does not change significantly (see Appendix).

A variety of diffusion-adsorption models are available to relate the rate of adsorption to diffusion coefficient, including the bidisperse model (Smith and Williams, 1984), the unipore model (Crank, 1975), and their modified versions (Cui et al., 2004; Clarkson and Bustin, 1999) that consider real adsorbent characteristics such as non-linear adsorption isotherms, time-varying boundary conditions. Nevertheless, all these models have made strong assumptions on the structure of the adsorbent (e.g., unimodal, bimodal). To avoid this artifact, the volumetric flow flux, J_v through a collection of pores is derived to be a product of the kinetic parameter (a direct experimental variable), and the molar density of the adsorbate is as follows:

$$J_v = R_{ads} V_m m_{sam} / A \tag{14}$$

where R_{ads} is the measured rate of adsorption, m_{sam} is the mass of the testing sample, V_m is the molar density of the flowing gas at standard condition, A is the cross-sectional area of the diffusion flow. Details of the calculation can be found in the Appendix.

R_{ads} is determined by taking the uptake adsorption amount of the adsorption isotherm averaged over the equilibrium time, which is readily accessible from adsorption kinetics curves (Fig. S1). As described in the preceding part, R_{ads} and the corresponding flow flux are evaluated on the basis of the surface excess quantity. For a scale-independent measure of the flow capacity, flow flux, J_v is calculated as a ratio of volumetric flow rate, q_t to the conducting area involved, A. This includes all connecting void spaces within the crushed sample.

Theoretical analysis is conducted to predict the flow flux as a function of pressure. Critical input parameters in the unified gas transport model are summarized in Table 2. Before the initiation of gas permeation, thermal equilibrium is assumed in the sample cell. This corresponds to an upstream boundary condition: constant gas concentration at the external surface of the crushed sample. As such, the flow considered starts when thermal equilibrium is attained after dosing gas molecules and terminates when they get adsorbed onto the pore surface. The cross-sectional area consists of conducting voids of different sizes, as depicted in Fig. 3, and the associated heterogeneity in the porosity distribution is characterized by low-pressure N_2 adsorption isotherm (Fig. 4). The net length of the flow streamline is considered to be the radius of the shale particles (~105 nm), where the streamline extends from exterior surface to center of the particle. Cylindrical pores are assumed because the length of a single channel is much larger than the pore scale involved. The pressure difference between upstream and downstream is quantified by the measured differential pressure ($\Delta P(t)$), and the outlet pressure is the gas pressure attained at adsorption equilibrium, P_e.

As expected, Fig. 10 shows a general agreement between the measured and modeled flow flux as a function of pore pressure when interactions between different flow mechanisms were properly considered. The resulting flow flux exhibits a monotonically decreasing trend with increasing pressure. Particularly, mass transport contribution from Knudsen flow reduces at higher pressures with more frequent intermolecular collisions, whereas its viscous slip counterpart increases with pressure. The modeling results exhibit some degrees of errors for pressures exceeding 3 MPa, potentially caused by changes in pore accessibility as adsorbed layers build up. The model domain is considered to be Marcellus shale where pore volume occupied by adsorbed layers is negligible at pressures investigated. Although a modification for adsorbed volume may provide a remedy for this discrepancy, it requires extensive modeling for the size and structure of the adsorbed phase that cannot be experimentally measured (Sircar, 1999).

Overall, we observe the dominance of viscous slip flux (contributing to at least 70 % of mass transport) in CH_4 flow through the EGSP shale at pressures investigated and beyond. Both slip flow and Knudsen diffusion occur as a result of wall or confinement effects, but the distinction and interaction between the two mechanisms are rarely recognized. A direct consequence is that one of them is ignored in predicting nanofluidic transport, as hypothesized in the Klinkenberg approach (Klinkenberg, 1941) or the apparent permeability model (Javadpour et al., 2007). To further assess the significance of considering both flow regimes, a comparative analysis is then proceeded with calculating flow flux in the absence of slip flow or Knudsen diffusion. Fig. 11 shows the resulting flow flux curve, where the failure to include slip flow greatly underestimates the actual flow flux whereas the exclusion of Knudsen diffusion leads to noticeable errors at low pressures (<3 MPa). Another observation is that the differences between predictions considering and not considering momentum transfer between Knudsen layer and viscous stream are found to be small in most conditions. This is highlighted in Fig. 11, showing closely spaced curves when slip-Knudsen or viscous-Knudsen interaction is neglected, despite some differences at low pressures.

In this section, we successfully applied the unified gas transport

Table 2
Pore dimensions and gas properties for methane permeation in EGSP shale.

Flow parameter	EGSP shale
Pore size distribution	Right-skewed
Mean pore diameter, d	9.7 nm
Length, L	105 μm
Temperature, T	303 K
Pressure difference or differential pressure readings	$\Delta P(t)$
Outlet pressure, P_{out}	P_e
Gas species	CH_4
Molecular mass, M	16 g/gmole

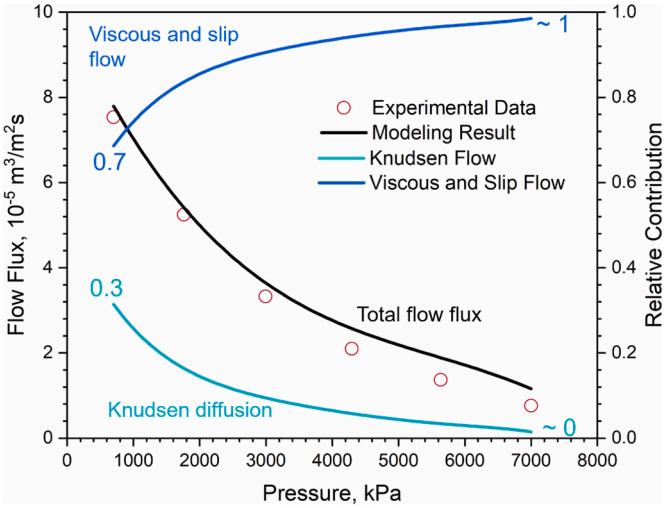

Fig. 10. Modeling and experimental results on methane flow flux in EGSP shale.

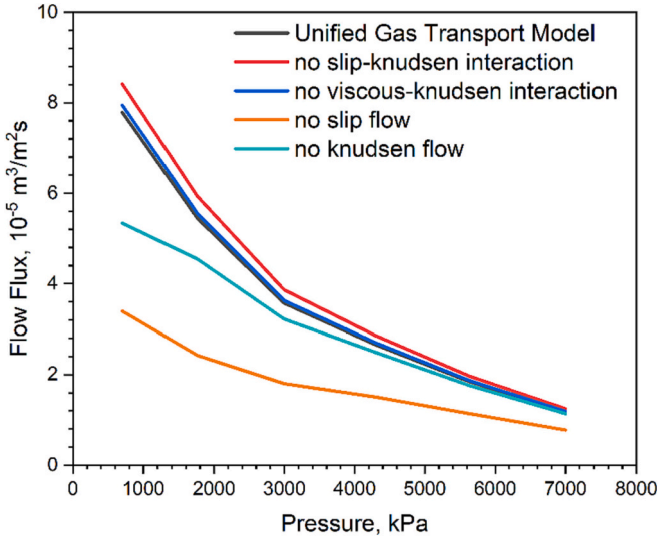

Fig. 11. Comparison of predictions on flow flux with and without considering viscous slip flow, Knudsen diffusion and their interactions.

model to predict methane flow flux at different reservoir pressures and identify the underlying flow mechanisms in shale gas production. This provides the essential theoretical foundation to quantify methane emissions potential for abandoned shale gas wells with long production history and low reservoir pressures.

4.3. *Fugitive methane emissions for abandoned shale gas wells*

After well abandonment, fugitive emissions continue at the well site, where abandoned wells are likely to act as potential contamination pathways to atmosphere and groundwater aquifers (if unplugged or well integrity is compromised) (Kang et al., 2014). This is particularly true for abandoned shale gas wells because the low recovery factor in these unconventional wells leaves significant gas reserves behind that become potential methane emission sources. To assess the emission potential, identifying the underlying flow mechanism of methane migration through the nanoporous shale matrix is of utmost importance. After well abandonment, reservoir pressure starts to equilibrate, and as a result, no significant pressure differential is expected to present across the reservoir. For this reason, Knudsen diffusion, driven by the concentration difference between gas-rich matrix and fracture network, is expected to be the dominant mechanism behind methane leakage from nanoporous shale matrix in abandoned wells. The other two flow regimes (viscous and slip flow) are passive advection flow, requiring pressure gradient to drive the flow, and therefore become inefficient in depleted reservoirs.

The unified gas transport model was applied to determine the mass flux under Knudsen diffusion. It is found that methane diffusive flux increases as reservoir pressure decreases. In particular, the diffusive flux becomes negligible when reservoir pressure is above 5 MPa. When applying the unified gas transport model to the measured methane gas transport data, the estimated diffusive volumetric flux increases from 2.5×10^{-8} to 3.8×10^{-7} m^3/m^2s as pressure decreases from 7 MPa to 0.7 MPa (see Fig. 11). Considering a typical shale gas well spacing of 400 m and a matrix porosity of 5 %, we estimate that methane emissions due to diffusive transport from shale matrix at 3×10^3 to 19×10^3 m^3 per well per day, which is comparable to methane emissions from the flowback fluid (~41 to 680×10^3 m^3 per well per day (Howarth et al., 2011)). Unlike the flow-back emissions and other methane emissions during well operation, the diffusion emissions have a long-lasting effect that accumulates over time. Therefore, it is important to incorporate diffusive flux from shale matrix as a significant methane emission source in the greenhouse gas inventory calculation for abandoned shale gas wells. Another important finding is that methane emission potential due to diffusive transport can be greatly diminished if sufficient reservoir pressure is maintained in abandoned shale gas wells. Reservoir pressure maintenance approaches such as injecting fluid into reservoir voidage should be considered by operators before well abandonment.

5. Conclusions

We propose an analytical model to estimate methane emission potential of abandoned shale gas wells, focusing on the remaining gas reserve in shale matrix. Specifically, a unified gas transport model is developed based on theoretical framework of kinetic theory to describe multi-scale gas transport in nanoporous media. The outcome of this work allows for the quantitative prediction of flow flux as a function of pore structure parameters and reservoir pressures, which is valuable for predicting diffusive methane flux and estimating methane emission potential of abandoned shale gas wells. This framework also offers a valuable approach to understanding the mass transport in nanoporous materials, which is relevant to questions in catalysis, energy storage, and beyond.

According to our analysis, we made the following conclusions.

1) The relative contribution of Knudsen diffusion, slip and viscous flow to total mass transfer is strongly dependent on pore pressure. As pressure decreases, Knudsen diffusion increases because more gas molecules collide with pore wall.
2) In shale formations, the driving force of Knudsen diffusion is the concentration difference between gas-rich matrix and fracture network, whereas viscous flow and slip flow are driven by the pressure difference across the reservoir. A large fraction of methane emissions from abandoned shale gas wells are due to diffusive transport of methane from shale matrix, where Knudsen diffusion acts as the primary leakage mechanism.
3) For the first time, a direct measurement of methane emission potential of abandoned shale gas wells is provided. We estimate methane emissions from diffusive flux at 3×10^3 to 19×10^3 m^3 per well per day, which is comparable to the largest emission during well operation (flow-back emissions) at 41×10^3 to 680×10^3 m^3 per well per day.

Our study provides an analytical tool to estimate methane emission potential of abandoned shale gas wells, focusing on diffusive flux from remaining gas reserve in shale matrix. For the first time, unrecovered natural gas in shale matrix is demonstrated to be a main source of

methane emissions from abandoned shale gas wells. Therefore, improving shale gas recovery factor through secondary or tertiary recovery methods are recommended as effective methane mitigation techniques. Orphaned shale gas wells, which are a category of unplugged nonproducing wells, need to be properly documented with reservoir attributes so that our proposed tool can estimate diffusion methane influx from unrecovered shale gas reserve over time. For plugged abandoned wells, research in various plug-in techniques should be further advanced in terms of preventing methane leakage via diffusion. The observed inverse relationship between diffusion flux and pore pressure suggests that maintaining reservoir pressure emerges as an effective strategy to reduce methane emission potential from abandoned shale gas wells. Given the long-lasting nature of diffusive transport to shale gas seepage, it is suggested that regulatory policies should be implemented to provide long-term monitoring of methane emissions from abandoned shale gas wells.

Nomenclature

A	Cross sectional area, m^2
$\bar{c}$	Mean molecular velocity, m/s
d	Pore diameter, m
f_{wall}	Fraction of wall collisions, dimensionless
$f(P)$	Fraction of gas molecules leaving the viscous stream, dimensionless
$F(t)$	Fraction of gas molecules flowing into the nanopores, dimensionless
J_v	Volumetric flow flux, $m^3/(m^2 \cdot s)$
k_t, k_k, k_v	Effective permeability corresponding to flow under transitional, pure Knudsen, and pure viscous flow regimes, md
L	Length of travelling path, m
M	Molecular weight, g/gmole
m_{sam}	Sample mass, g
N_{wall}	Total number of molecules impinging upon a unit length of wall per unit time, mole/m
$N_{molecule}$	Total number of intermolecular collisions per unit time per unit length of wall, mole/m
n	Molar density, $mole/m^3$
P	Pore pressure, Pa
P_{in}, P_{out}	Inlet and outlet pressure, kPa
P_e	Adsorption equilibrium pressure, kPa
$\Delta P(t)$	Transient differential pressure readings, Pa
ΔP_e	Differential pressure at adsorption equilibrium, Pa
dP/dL	Pressure gradient, Pa/m
q_v	Volumetric gas rate due to viscous flow, m^3/s
q_s	Volumetric flow rate due to slip flow, m^3/s
q_k	Volumetric flow rate due to Knudsen diffusion, m^3/s
q_t	Total volumetric flow rate due to viscous, slip and Knudsen diffusion flow, m^3/s
R	Gas constant, 8.314 $m^3 \cdot Pa/(K \cdot mol)$
R_{ads}	Rate of adsorption, mmole/(g·s)
T	Temperature, K
u_s, u_w	Slip and wall velocity, respectively, m/s
V_{sr}, V_{rr}	Cell volume of charging cells at the sample and reference sides, respectively, m^3
V_{ss}, V_{sr}	Cell volume of sample cells at sample and reference sides, respectively, m^3
V_s	Sample volume, m^3
V_m	Molar volume at standard condition, 22.4e−5 m^3/mmole
x_{min}, x_{max}	Lower and upper bound for pore size distribution, m
Z_s, Z_e	Gas compressibility factor corresponding to transient and equilibrium pressures, respectively, dimensionless
μ	Viscosity, Pa·s
λ	Mean free path, m
σ_v	Tangential momentum accommodation coefficient, dimensionless
$\rho(d)$	Pore size distribution

CRediT authorship contribution statement

Yun Yang: Conceptualization, Data curation, Formal analysis, Investigation, Methodology, Resources, Software, Validation, Visualization, Writing – original draft, Writing – review & editing. **Shimin Liu:** Conceptualization, Data curation, Formal analysis, Funding acquisition, Investigation, Methodology, Project administration, Resources, Software, Supervision, Validation, Visualization, Writing – original draft, Writing – review & editing. **Haoming Ma:** Conceptualization, Formal analysis, Resources, Visualization, Writing – original draft, Writing – review & editing.

Declaration of competing interest

The authors declare that they have no known competing financial interests or personal relationships that could have appeared to influence the work reported in this paper.

Data availability

Data will be made available on request.

Appendix A. Supplementary data

Supplementary data to this article can be found online at https://doi.org/10.1016/j.scitotenv.2023.169750.

References

Azom, P.N., Javadpour, F., 2012. Dual-continuum modeling of shale and tight gas reservoirs. In: SPE Annual Technical Conference and Exhibition. Society of Petroleum Engineers.

Barrett, E.P., Joyner, L.G., Halenda, P.P., 1951. The determination of pore volume and area distributions in porous substances. I. Computations from nitrogen isotherms. J. Am. Chem. Soc. 73 (1), 373–380. https://doi.org/10.1021/ja01145a126.

Beskok, A., Karniadakis, G.E., 1999. Report: a model for flows in channels, pipes, and ducts at micro and nano scales. Microscale Thermophys. Eng. 3 (1), 43–77.

Bird, R.B., Stewart Warren, E., 2007. Lightfoot Edwin N, Transport Phenomena. John Wiley & Sons, New York, NY.

Bosanquet, C.H., 1944. British TA Report BR-507.

Boutot, J., Peltz, A.S., McVay, R., Kang, M., 2022. Documented orphaned oil and gas wells across the United States. Environ. Sci. Technol. 56 (20), 14228–14236.

Brace, W.F., Walsh, J., Frangos, W., 1968. Permeability of granite under high pressure. J. Geophys. Res. 73 (6), 2225–2236.

Bravo, M.C., 2007. Effect of transition from slip to free molecular flow on gas transport in porous media. J. Appl. Phys. 102 (7), 074905.

Caulton, D.R., Shepson, P.B., Santoro, R.L., Sparks, J.P., Howarth, R.W., Ingraffea, A.R., Cambaliza, M.O.L., Sweeney, C., Karion, A., Davis, K.J., Stirm, B.H., Montzka, S.A., Miller, B.R., 2014. Toward a better understanding and quantification of methane emissions from shale gas development. Proc. Natl. Acad. Sci. 111 (17), 6237–6242. https://doi.org/10.1073/pnas.1316546111.

Chandra, D., Vishal, V., Bahadur, J., Sen, D., 2020. A novel approach to identify accessible and inaccessible pores in gas shales using combined low-pressure sorption and SAXS/SANS analysis. Int. J. Coal Geol. 228, 103556.

Civan, F., Rai, C.S.S., Sondergeld, C.H.H., 2012. Determining shale permeability to gas by simultaneous analysis of various pressure tests. SPE J. 17 (03), 717–726. https://doi.org/10.2118/144253-pa.

Clarkson, C.R., Bustin, R.M., 1999. The effect of pore structure and gas pressure upon the transport properties of coal: a laboratory and modeling study. 2. Adsorption rate modeling. Fuel 78 (11), 1345–1362.

Clarkson, C.R., Solano, N., Bustin, R.M., Bustin, A.M.M., Chalmers, G.R.L., He, L., Melnichenko, Y.B., Radliński, A.P., Blach, T.P., 2013. Pore structure characterization of North American shale gas reservoirs using USANS/SANS, gas adsorption, and mercury intrusion. Fuel 103, 606–616. https://doi.org/10.1016/j.fuel.2012.06.119.

Crank, J., 1975. The Mathematics of Diffusion, Oxford. Clarendon Press, GB.

Cui, X., Bustin, R.M., Dipple, G., 2004. Selective transport of CO2, CH4, and N2 in coals: insights from modeling of experimental gas adsorption data. Fuel 83 (3), 293–303. https://doi.org/10.1016/j.fuel.2003.09.001.

Cui, X., Bustin, A., Bustin, R.M., 2009. Measurements of gas permeability and diffusivity of tight reservoir rocks: different approaches and their applications. Geofluids 9 (3), 208–223.
Darabi, H., Ettehad, A., Javadpour, F., Sepehrnoori, K., 2012. Gas flow in ultra-tight shale strata. J. Fluid Mech. 710, 641–658. https://doi.org/10.1017/jfm.2012.424.
Dongari, N., Zhang, Y., Reese, J.M., 2011. Modeling of Knudsen layer effects in micro/nanoscale gas flows. J. Fluids Eng. 133 (7) https://doi.org/10.1115/1.4004364.
Dubbeldam, D., Snurr, R.Q., 2007. Recent developments in the molecular modeling of diffusion in nanoporous materials. Mol. Simul. 33 (4–5), 305–325. https://doi.org/10.1080/08927020601156418.
Dyman, T.S., Wilcox, L.A., 1983. The Eastern Gas Shales Project (EGSP) data system: a case study in data base design, development, and application. J. Int. Assoc. Math. Geol. 15 (2), 363–369. https://doi.org/10.1007/BF01036076.
Egermann, P., Lenormand, R., Longeron, D., Zarcone, C., 2005. A fast and direct method of permeability measurements on drill cuttings. SPE Reserv. Eval. Eng. 8 (04), 269–275. https://doi.org/10.2118/77563-pa.
EIA, 2022. Annual Energy Outlook 2022: With Projections to 2050. Energy Informtation Administration.
EPA, 2023. Inventory of U.S. Greenhouse Gas Emissions and Sinks: 1990–2021., in: U.S. E.P. Agency (Ed.) EPA 430-R-23-002. https://www.epa.gov/ghgemissions/inventory-us-greenhouse-gas-emissions-and-sinks-1990-2021.
Ertekin, T., King, G.A., Schwerer, F.C., 1986. Dynamic gas slippage: a unique dual-mechanism approach to the flow of gas in tight formations. SPE-12258-PA 1 (01), 43–52. https://doi.org/10.2118/12045-PA.
Evans III, R., Watson, G., Mason, E., 1961. Gaseous diffusion in porous media at uniform pressure. J. Chem. Phys. 35 (6), 2076–2083.
Goodbody, S.J., Watanabe, K., Macgowan, D., Walton, J.P.R.B., Quirke, N., 1991. Molecular simulation of methane and butane in silicalite. J. Chem. Soc. Faraday Trans. 87 (13), 1951. https://doi.org/10.1039/ft9918701951.
Hagen, G., 1839. Ueber die Bewegung des Wassers in engen cylindrischen Röhren. Ann. Phys. 122 (3), 423–442. https://doi.org/10.1002/andp.18391220304.
Heller, R., Vermylen, J., Zoback, M., 2014. Experimental investigation of matrix permeability of gas shales. AAPG Bull. 98 (5), 975–995. https://doi.org/10.1306/09231313023.
Howarth, R.W., Santoro, R., Ingraffea, A., 2011. Methane and the greenhouse-gas footprint of natural gas from shale formations. Clim. Chang. 106 (4), 679–690. https://doi.org/10.1007/s10584-011-0061-5.
IEA, 2023. Global Methane Tracker 2023. IEA, Paris.
IPCC, 2022. Summary for policymakers. In: C. Intergovernmental Panel on Climate (Ed.), Climate Change 2022 - Mitigation of Climate Change: Working Group III Contribution to the Sixth Assessment Report of the Intergovernmental Panel on Climate Change. Cambridge University Press, Cambridge, UK, pp. 3–48. https://doi.org/10.1017/9781009157926.001.
Javadpour, F., 2009. Nanopores and Apparent Permeability of Gas Flow in Mudrocks (Shales and Siltstone). https://doi.org/10.2118/09-08-16-DA.
Javadpour, F., Fisher, D., Unsworth, M., 2007. Nanoscale gas flow in shale gas sediments. J. Can. Pet. Technol. 46 (10) https://doi.org/10.2118/07-10-06.
Javadpour, F., Moravvej Farshi, M., Amrein, M., 2012. Atomic-force microscopy: a new tool for gas-shale characterization. J. Can. Pet. Technol. 51 (04), 236–243. https://doi.org/10.2118/161015-PA.
Jeans, J.H., 1921. The Dynamical Theory of Gases. University Press.
Kang, M., Kanno, C.M., Reid, M.C., Zhang, X., Mauzerall, D.L., Celia, M.A., Chen, Y., Onstott, T.C., 2014. Direct measurements of methane emissions from abandoned oil and gas wells in Pennsylvania. Proc. Natl. Acad. Sci. 111 (51), 18173–18177. https://doi.org/10.1073/pnas.1408315111.
Kang, M., Christian, S., Celia, M.A., Mauzerall, D.L., Bill, M., Miller, A.R., Chen, Y., Conrad, M.E., Darrah, T.H., Jackson, R.B., 2016. Identification and characterization of high methane-emitting abandoned oil and gas wells. Proc. Natl. Acad. Sci. 113 (48), 13636–13641.
Kang, M., Boutot, J., McVay, R.C., Roberts, K.A., Jasechko, S., Perrone, D., Wen, T., Lackey, G., Raimi, D., Digiulio, D.C., Shonkoff, S.B.C., William Carey, J., Elliott, E.G., Vorhees, D.J., Peltz, A.S., 2023. Environmental risks and opportunities of orphaned oil and gas wells in the United States. Environ. Res. Lett. 18 (7), 074012 https://doi.org/10.1088/1748-9326/acdae7.
Kärger, J., Ruthven, D.M., Theodorou, D.N., 2012. Diffusion in Nanoporous Materials. John Wiley & Sons.
Karion, A., Sweeney, C., Pétron, G., Frost, G., Michael Hardesty, R., Kofler, J., Miller, B. R., Newberger, T., Wolter, S., Banta, R., 2013. Methane emissions estimate from airborne measurements over a western United States natural gas field. Geophys. Res. Lett. 40 (16), 4393–4397.
Katsaros, F.K., Steriotis, T.A., Stubos, A.K., Mitropoulos, A., Kanellopoulos, N.K., Tennison, S., 1997. High pressure gas permeability of microporous carbon membranes. Microporous Mater. 8 (3), 171–176. https://doi.org/10.1016/S0927-6513(96)00080-6.
Kennard, E.H., 1938. Kinetic Theory of Gases : With an Introduction to Statistical Mechanics, 1st ed. McGraw-Hill New York, New York.
Kholod, N., Evans, M., Pilcher, R.C., Roshchanka, V., Ruiz, F., Coté, M., Collings, R., 2020. Global methane emissions from coal mining to continue growing even with declining coal production. J. Clean. Prod. 256, 120489.
Klinkenberg, L.J., 1941. The Permeability of Porous Media to Liquids and Gases. American Petroleum Institute, New York, New York, Drilling and Production Practice, p. 14.
Liu, Q., Shen, P., Yang, P., 2002. Pore scale network modelling of gas slippage in tight porous media. In: Chen, Z., Ewing, R.E. (Eds.), Fluid Flow and Transport in Porous Media: Mathematical and Numerical Treatment, Contemporary Mathematics, pp. 367–376. https://doi.org/10.1090/conm/295.
Luffel, D.L., Hopkins, C.W., Schettler Jr., P.D., 1993. Matrix permeability measurement of gas productive shales. In: SPE Annual Technical Conference and Exhibition. Society of Petroleum Engineers, Houston, Texas, p. 10.
Ma, H., Yang, Y., Zhang, Y., Li, Z., Zhang, K., Xue, Z., Zhan, J., Chen, Z., 2022. Optimized schemes of enhanced shale gas recovery by CO2-N2 mixtures associated with CO2 sequestration. Energy Convers. Manag. 268.
Mason, E.A., Malinauskas, A., 1983. Gas Transport in Porous Media: The Dusty-gas Model. Elsevier Science Ltd.
Maxwell, J.C., 1965. The Scientific Papers of James Clerk Maxwell. Dover Publication Inc., Mineola New York.
Middleton, R.S., Carey, J.W., Currier, R.P., Hyman, J.D., Kang, Q., Karra, S., Jiménez-Martínez, J., Porter, M.L., Viswanathan, H.S., 2015. Shale gas and non-aqueous fracturing fluids: opportunities and challenges for supercritical CO2. Appl. Energy 147, 500–509. https://doi.org/10.1016/j.apenergy.2015.03.023.
Miller, B., 2015. 8 - greenhouse gas – carbon dioxide emissions reduction technologies. In: Miller, B. (Ed.), Fossil Fuel Emissions Control Technologies. Butterworth-Heinemann, pp. 367–438. https://doi.org/10.1016/B978-0-12-801566-7.00008-7.
Mistler, T.E., Correll, G.R., Mingle, J.O., 1970. Gaseous diffusion in the transition pressure range. AIChE J 16 (1), 32–37. https://doi.org/10.1002/aic.690160108.
Myhre, G., Shindell, D., Bréon, F., Collins, W., Fuglestvedt, J., Huang, J., Koch, D., Lamarque, J., Lee, D., Mendoza, B., 2013. Climate change 2013: the physical science basis. In: Contribution of Working Group I to the Fifth Assessment Report of the Intergovernmental Panel on Climate Change. Cambridge University Press, Cambridge, UK.
Neil, C.W., Mehana, M., Hjelm, R.P., Hawley, M.E., Watkins, E.B., Mao, Y., Viswanathan, H., Kang, Q., Xu, H., 2020. Reduced methane recovery at high pressure due to methane trapping in shale nanopores. Commun. Earth Environ. 1 (1), 49. https://doi.org/10.1038/s43247-020-00047-w.
Nisbet, E.G., Fisher, R.E., Lowry, D., France, J.L., Allen, G., Bakkaloglu, S., Broderick, T. J., Cain, M., Coleman, M., Fernandez, J., Forster, G., Griffiths, P.T., Iverach, C.P., Kelly, B.F.J., Manning, M.R., Nisbet-Jones, P.B.R., Pyle, J.A., Townsend-Small, A., al-Shalaan, A., Warwick, N., Zazzeri, G., 2020. Methane mitigation: methods to reduce emissions, on the path to the Paris Agreement. Rev. Geophys. 58 (1), e2019RG000675 https://doi.org/10.1029/2019RG000675.
Patzek, T.W., Male, F., Marder, M., 2013. Gas production in the Barnett Shale obeys a simple scaling theory. Proc. Natl. Acad. Sci. 110 (49), 19731–19736. https://doi.org/10.1073/pnas.1313380110.
Pétron, G., Frost, G., Miller, B.R., Hirsch, A.I., Montzka, S.A., Karion, A., Trainer, M., Sweeney, C., Andrews, A.E., Miller, L., 2012. Hydrocarbon emissions characterization in the Colorado Front Range: a pilot study. J. Geophys. Res. Atmos. 117 (D4).
Purewal, J., Kabbour, H., Vajo, J., Ahn, C., Fultz, B., 2009. Pore size distribution and supercritical hydrogen adsorption in activated carbon fibers. Nanotechnology 20 (20), 204012.
Roy, S., Raju, R., Chuang, H.F., Cruden, B.A., Meyyappan, M., 2003. Modeling gas flow through microchannels and nanopores. J. Appl. Phys. 93 (8), 4870–4879. https://doi.org/10.1063/1.1559936.
Schmoker, J.W., 1980. Organic Content of Devonian Shale in Western Appalachian Basin. AAPG Bull. 64 (12), 2156–2165. https://doi.org/10.1306/2f919756-16ce-11d7-8645000102c1865d.
Scott, D.S., Dullien, F.A.L., 1962. Diffusion of ideal gases in capillaries and porous solids. AIChE J 8 (1), 113–117. https://doi.org/10.1002/aic.690080126.
Singh, A.K., Singh, U., Panigrahi, D.C., Singh, J., 2022. Updated greenhouse gas inventory estimates for Indian underground coal mining based on the 2019 IPCC refinements. Iscience 25 (9).
Sircar, S., 1999. Gibbsian surface excess for gas adsorption revisited. Ind. Eng. Chem. Res. 38 (10), 3670–3682. https://doi.org/10.1021/ie9900871.
Smith, D.M., Williams, F.L., 1984. Diffusional effects in the recovery of methane from coalbeds. Soc. Pet. Eng. J. 24 (05), 529–535.
Sudibandriyo, M., Pan, Z., Fitzgerald, J.E., Robinson, R.L., Gasem, K.A.M., 2003. Adsorption of methane, nitrogen, carbon dioxide, and their binary mixtures on dry activated carbon at 318.2 K and pressures up to 13.6 MPa. Langmuir 19 (13), 5323–5331. https://doi.org/10.1021/la020976k.
Thompson, S.L., Owens, W.R., 1975. A survey of flow at low pressures. Vacuum 25 (4), 151–156. https://doi.org/10.1016/0042-207X(75)91404-9.
Trimmer, D., Bonner, B., Heard, H.C., Duba, A., 1980. Effect of pressure and stress on water transport in intact and fractured gabbro and granite. J. Geophys. Res. Solid Earth 85 (B12), 7059–7071. https://doi.org/10.1029/JB085iB12p07059.
Veldsink, J., Van Damme, R.M., Versteeg, G., Van Swaaij, W.P.M., 1995. The use of the dusty-gas model for the description of mass transport with chemical reaction in porous media. Chem. Eng. J. 57 (2), 115–126.
Vincenti, W.G., Kruger, C.H., 1965. Introduction to Physical Gas Dynamics. Krieger Publishing Company.
Vishal, V., Singh, L., Pradhan, S.P., Singh, T.N., Ranjith, P., 2013. Numerical modeling of Gondwana coal seams in India as coalbed methane reservoirs substituted for carbon dioxide sequestration. Energy 49, 384–394.
Wu, K., Chen, Z., Li, X., 2015. Real gas transport through nanopores of varying cross-section type and shape in shale gas reservoirs. Chem. Eng. J. 281, 813–825. https://doi.org/10.1016/j.cej.2015.07.012.
Yamada, S.E., Jones, A.H., 1980. A review of a pulse technique for permeability measurements. Soc. Pet. Eng. J. 20 (05), 357–358. https://doi.org/10.2118/8760-pa.

Yang, Y., Liu, S., 2019. Estimation and modeling of pressure-dependent gas diffusion coefficient for coal: a fractal theory-based approach. Fuel 253, 588–606. https://doi.org/10.1016/j.fuel.2019.05.009.

Yang, Y., Liu, S., 2020. Laboratory study of cryogenic treatment induced pore-scale structural alterations of Illinois coal and their implications on gas sorption and diffusion behaviors. J. Pet. Sci. Eng. 194, 107507 https://doi.org/10.1016/j.petrol.2020.107507.

Yang, Y., Liu, S., Clarkson, C., 2022. Quantification of temperature-dependent sorption isotherms in shale gas reservoirs: experiment and theory. SPE J. 27 (05), 3001–3019. https://doi.org/10.2118/205897-pa.

Yu, W., Sepehrnoori, K., Patzek, T.W., 2016. Modeling gas adsorption in Marcellus Shale with Langmuir and BET isotherms. SPE J. 21 (02), 589–600. https://doi.org/10.2118/170801-PA.